Journal of Hazardous Materials 424 (2022) 127348

Contents lists available at ScienceDirect

Journal of Hazardous Materials

journal homepage: www.elsevier.com/locate/jhazmat

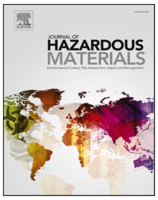

Nitrogen-rich layered carbon for adsorption of typical volatile organic compounds and low-temperature thermal regeneration

Li Tan [a], Jiangen Wang [a], Bihai Cai [a], Chengyin Wang [b], Zhimin Ao [a,*], Shaobin Wang [c]

[a] *Guangzhou Key Laboratory of Environmental Catalysis and Pollution Control, Guangdong Key Laboratory of Environmental Catalysis and Health Risk Control, School of Environmental Science and Engineering, Institute of Environmental Health and Pollution Control, Guangdong University of Technology, Guangdong 510006, China*
[b] *College of Chemistry and Chemical Engineering, Jiangsu Key Laboratory of Environmental Engineering and Monitoring, Yangzhou University, Yangzhou 225002, China*
[c] *School of Chemical Engineering and Advanced Materials, the University of Adelaide, Adelaide, SA 5005, Australia*

ARTICLE INFO

Editor: Prof. Jörg Rinklebe

Keywords:
VOCs
Adsorption
Nitrogen-rich carbon
Desorption
Regeneration

ABSTRACT

Carbon-based adsorbents with a high adsorption capacity and low price have been widely used in the removal of volatile organic compounds (VOCs), but the poor gas selectivity and reusability limit their industrial applications. In this work, disc-like nitrogen-rich porous carbon materials (HAT-Xs) were synthesized to remove typical VOCs via adsorption. By controlling the synthesis temperature from 450 to 1000 °C, the C/N ratio of the HAT-Xs increased from 1.85 to 12.56. The HAT-650 synthesized at 650 °C with the high specific surface area of 305 m^2 g^{-1} exhibits the highest adsorption capacity of 141 mg g^{-1} for ethyl acetate (which is 3.2 times for that of activated carbon), and 39.4 mg g^{-1} for n-hexane, 48.6 mg g^{-1} for toluene. Kinetic studies indicated that the adsorption is physical adsorption and that the interior surface diffusion is the main rate-determining step during the adsorption progress, the interior surface diffusion rate of ethyl acetate on HAT-650 is 1.455 mg g^{-1} $min^{-0.5}$. At the same time, the desorption and reuse tests show that HAT-650 has excellent reusability with low desorption and regeneration temperature of 120 °C, and high desorption efficiency of 95.2% and that it could be a promising ethyl acetate adsorbent for industrial applications.

1. Introduction

Volatile organic compounds (VOCs) are classified as the organics with a boiling point below 250 °C, including benzene series, organic chlorides, Freon series, organic ketones, amines, alcohols, ethers, esters, acids, and petroleum hydrocarbon compounds (Gwenzi et al., 2021). With the development of industry and human society, the emission of VOCs is increasing year by year, while animals and plants emit pollutants, but human activities including industrial solvents and transportation are the most important sources of volatile pollutants (Qiu et al., 2014). In the past decades, VOCs have attracted worldwide attention and posed a major threat to public health (González-Martín et al., 2021). Researches show that most VOCs such as benzene, toluene, formaldehyde, n-hexane, and ethyl acetate are toxic to human health, and may even cause cancer and death (Sciorio et al., 2021; Davidson et al., 2021; Azhagapillai et al., 2020). Therefore, developing removal technologies for VOCs is an urgent challenge for researchers. Adsorption technology with low energy consumption, environment-friendliness, easy operation, no secondary pollution, and low cost has been widely used for VOCs removal (Gang et al., 2021). Moreover, a large amount of literature shows that adsorption is the first step of catalytic oxidation, essential for the catalytic transformation of VOC molecules (Yang et al., 2019; Liu et al., 2019).

An adsorbent is a key to adsorption technology, and various adsorbents have been reported for the adsorption of VOCs, including carbon-based materials, (Wang et al., 2012a) metal-organic frameworks (Guo et al., 2021), zeolites (Kim and Ahn, 2012), and silica gels (Yue et al., 2021), etc. Carbon-based materials have been recognized as one of the most economic and promising adsorbents for their high specific surface area, special pore structure, easy availability, and cheap price (Zhu et al., 2019). In the past researches, various kinds of carbon-based materials have been used as adsorbents to remove VOCs, including carbon nanotubes, activated carbon, carbon spheres, modified carbon materials, grapheme, and its derivatives, etc (Pan and Xing, 2008; Chabot et al., 2014; Zhou et al., 2014). In early 1998, Nguyen and Do (1998) compared the adsorption performance of activated carbon for benzene and ethanol. Later, fibrous carbonaceous materials, activated carbon fibers were used as toluene adsorbents (Oh et al., 2008). Biochar is also a

---

* Corresponding author.
E-mail address: zhimin.ao@gdut.edu.cn (Z. Ao).

https://doi.org/10.1016/j.jhazmat.2021.127348
Received 7 July 2021; Received in revised form 12 September 2021; Accepted 23 September 2021

kind of carbon material produced from biomass, with similar chemical and physical properties of activated carbon, and has been widely used in CO_2 sequestration, catalytic conversion of syngas into biodiesel, pollution remediation, and VOCs adsorption (Uchimiya et al., 2010; Zhang et al., 2017). However, typical carbon materials such as activated carbon and ordered mesoporous carbon have poor gas selectivity and long-term stability and are hard to regenerate after adsorption (Gang et al., 2021). In addition, the recovery and reuse efficiency of the adsorbed gas is not ideal, which limits the industrial applications of the carbon adsorbents. Desorption is of very practical significance for the recovery and reuse of adsorbed gas (Bathen, 2003). Heat treatment methods are widely used to release VOCs and regenerate adsorbents (Zheng et al., 2021). However, the desorption of most adsorbents requires a high temperature exceeding 200 °C. To obtain high temperature, high-quality equipment, and high energy consumption are required. The high costs caused by these are the bottlenecks of industrial applications.

Recently, N-doped carbon materials have been widely used in several areas, like oxygen evolution reaction (Kong et al., 2014), oxygen reduction reaction (Kong et al., 2014), CO_2 reduction (Zhang et al., 2020), and VOCs adsorption (Wang et al., 2015). The doping of N atom effectively modifies the electronic properties of carbon materials, which is beneficial for carriers mobility and provides active sites (Duan et al., 2017). Sun et al. (2020) and his group tested the BPA adsorption capacity of N-doped carbon and showed that increased N concentration can improve the adsorption performance of the carbon materials, due to the N atom with strong electronegativity could increase the π-acceptor capacity of carbon and improve the interaction with π-donor of BPA. You et al. (2021) found that the N-doped graphite layer can enhance the peroxymonosulfate adsorption and activation on NiZn@N-G-900. Through the experimental and DFT calculations, they discovered that N-doped graphite can change the surface charge distribution and improve the charge transfer between the catalyst and the adsorbate. Therefore, nitrogen doping is a potential method in terms of the adsorption of VOCs.

The nitrogen-doped carbon materials generated by traditional CVD and thermal treatment methods use graphite oxide, CH_4, and NH_3 gases as the precursors, their nitrogen content is usually below 10 at% (Wang et al., 2012b). In recent years, many nitrogenous precursors, including organic macromolecules, biomass, organic polymers, and MOFs, have been used for the preparation of nitrogen-doped carbon materials (Xu et al., 2020). These new kinds of nitrogen-doped carbons exhibit several unique features, such as large mesopores, high specific surface area, abundant surface functional groups, and high nitrogen content. In 2015, Mahmood et al. (2015), used hexaaminobenzene trihydrochloride and hexaketocyclohexane octahydrate as precursors synthesized a kind of 2D structures C_2N with regular pore structure, the high specific surface area of 281 $m^2\ g^{-1}$, and high nitrogen content of 33.3 at%. Kou et al. (2011) synthesized nitrogen-rich nanostructured carbon materials with precursors of 1,2,4,5-benzenetetramine and triquinoyl hydrate, which the BET surface area was as high as 1029 $m^2\ g^{-1}$ and the pore size was decreased to 0.9 nm. Walczak et al. (2018) synthesized a kind of N-rich nano-porous carbon materials with high specific surface area, abundant surface functional groups and high nitrogen content of 29.4 at%.

In this work, nitrogen-rich porous carbon materials from a precursor of hexaazatriphenylene-hexacarbonitrile (HAT-CN) were synthesized via a one-step carbonization process. By controlling the synthesis temperature, a series of nitrogen-rich carbon materials, HAT-Xs (X = 450, 650, 800, 900, and 1000), have been synthesized. Various characterizations have been used to study the physical and chemical properties of the adsorbents. The adsorption performance of the HAT-Xs for three typical VOCs (toluene, n-hexane, and ethyl acetate) were tested at ambient temperature. Compared with toluene and n-hexane, HAT-Xs show excellent adsorption to ethyl acetate, and kinetic studies show that the diffusion of ethyl acetate in HAT-650 is easier than toluene and n-hexane. Several mathematical models including pseudo-first-order model, pseudo-second-order model, intra-particle diffusion model, and Langmuir model were used to study the kinetic mechanism of the adsorption process. To test the stability of the materials, the cyclic test was also carried out. The sample HAT-650 shows excellent reusability with an adsorption capacity of 105.5 mg g^{-1} after nine cycles.

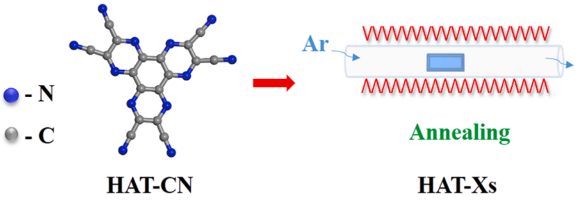

Fig. 1. Schematic illustration of the synthesis of HAT-Xs (X = 450, 650, 800, 900, 1000).

2. Materials and methods

2.1. Materials

Hexaketocyclohexane octahydrate (99%) was purchased from Beijing Innochem Technology Co., Ltd., China. Diaminomaleonitrile was provided by Shanghai Aladdin Biochemical Technology Co., Ltd., China. Acetic acid (AR, 99.5%), nitric acid (AR, 65%), and acetonitrile (AR) were supplied by Guangzhou Chemical Reagent Factory, China. An activated carbon used in this work was provided by Guangdong Guangsen Carbon Industry Technology Co., Ltd., China. All the reagents were used without further purification.

Hexaazatriphenylene-hexacarbonitrile (HAT-CN) materials were synthesized according to a typical method (Walczak et al., 2018; Li et al., 2019). Firstly, 4 g Hexaketocyclohexane octahydrate and 10.88 g diaminomaleonitrile were refluxed in 150 mL Acetic acid for 2 h. Secondly, the black solid was filtered off while hot and washed with hot Acetic acid (75 mL, ~100 ℃). Thirdly, the black solid was put into 60 mL 30% HNO_3 and heated at 100 ℃, and refluxed for 3 h. Then, the hot dark brown suspension was poured into ice water (200 mL) and cooled overnight. Next, the suspension was filtered and the red-brown solid was refluxed in 400 mL acetonitrile for 2 h. Finally, heat and evaporate the filtrate to obtain an orange solid.

HAT-X (X = 450, 650, 800, 900, 1000) were synthesized by a one-step carbonization process at different temperatures (450, 650, 800, 900, and 1000 °C) with the precursor of HAT-CN (as shown in Fig. 1). As an example, HAT-450 was prepared as follows: 1 g HAT-CN was put into a tubular furnace, and then heated to 450 °C with a heating rate of 5 °C /min, under Ar atmosphere and kept for 2 h.

2.2. Characterizations

Powder X-ray diffraction (XRD) patterns were performed on a D/MAX-Ultima IV X-ray diffractometer (Rigaku, Japan) with Cu Kα irradiation (λ = 1.5406 Å) by a scan rate of 4°/min. Scanning electron microscopy (SEM) was observed using SU8220 (Hitach, Japan) with a high voltage of 15 kV, and equipped with an energy dispersive X-ray spectrometer (EDS). Transmission electron microscopy (TEM) was performed on a Talos F200s with an accelerating voltage of 100 kV. X-ray photoelectron spectroscopy (XPS) data were obtained by an ESCALABMk 250Xi spectrometer with a C 1 s reference peak at 284.6 eV. The Brunauer-Emmett-Teller (BET) surface areas were determined by N_2 sorption using a BELMaster analyzer. Raman spectra were obtained on a LabRAM HR800 Raman spectrometer equipped with a 532 nm Ar^+ laser (Horiba Jobin-Yvon). Thermal stabilities analysis of the samples were performed by a thermal gravimetric and simultaneous heat-infrared spectroscopy combined system (TGA-IR, TGA/DSC3 +, FTIR/Nicolet IS 50) with the temperature of 20–1000 °C and infrared spectroscopy at a range of 4000–500 cm^{-1}.

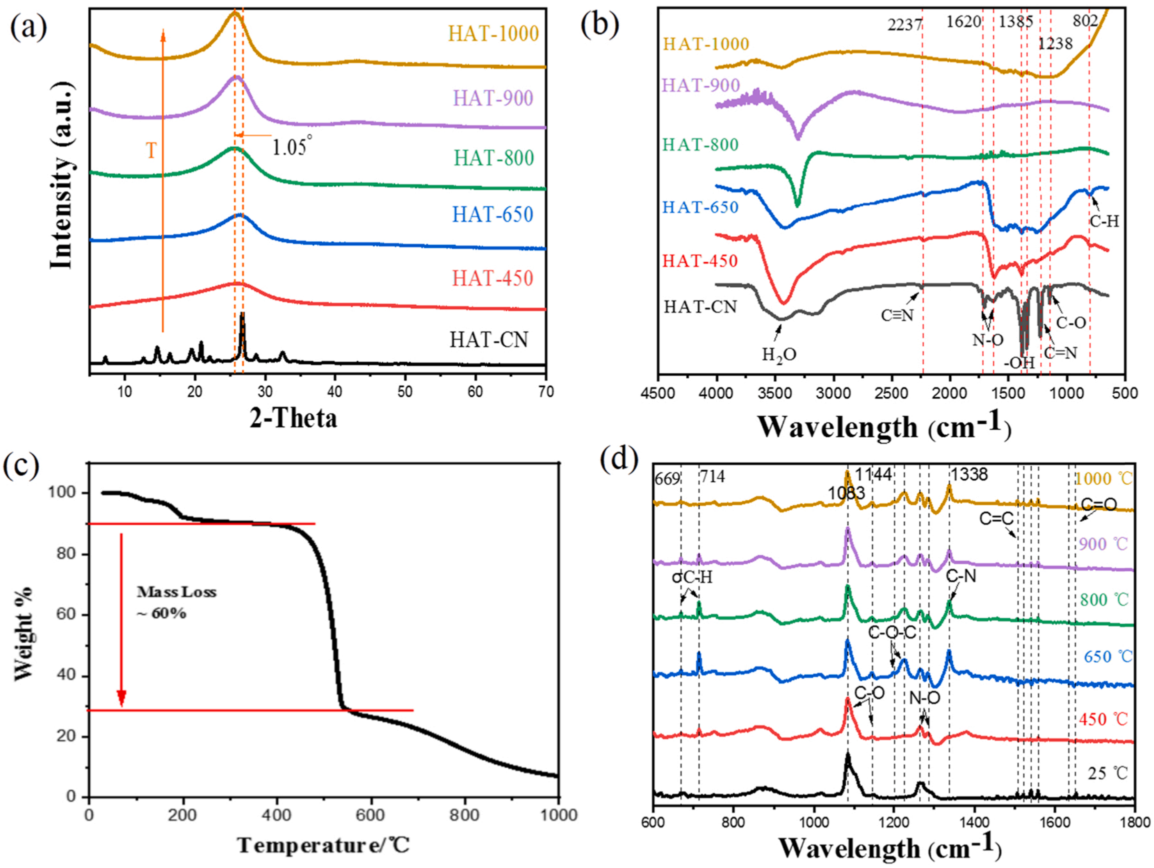

Fig. 2. (a) XRD spectra and (b) FT-IR spectra of HAT-CN, HAT-450, HAT-650, HAT-800, HAT-900 and HAT-1000, (c) TGA profile of HAT-CN, (d) IR transmission spectra of the vapor release from pure HAT-CN.

2.3. *Adsorption measurements*

2.3.1. *Adsorption experiments*

The adsorption experiments were conducted in a gas distributing system providing the gases in a continuous flow mode. During the adsorption process, 50 mg of the as-synthesized sample was filled in a customer-made cylindrical quartz glass reactor (φ = 6 mm). The inlet concentration was 150 ± 5 ppm and the total flow was 30 mL/min with the gas hourly space velocity of ~16,000 h^{-1}. Gas was sampled at given intervals with an auto-feeding device, and the gas sample (1 mL) was injected into gas chromatography (Shanghai Kechuang Chromatographic Instrument Co. Ltd, China) with a capillary column (30 m × 0.32 mm × 0.5 μm) for concentration determination. Each group sample was tested at least 3 times to calculate mean and error. In this work, we used 3 kinds of VOCs, ethyl acetate, toluene, and n-hexane, as the target pollutant gases. During the adsorption test, 9 mL/min flow of 500 ppm VOCs and 21 mL/min high purity (99.999%) nitrogen passed into a high-pressure tank, respectively. Then the concentration of ethyl acetate in the mixture gas stabilized at 150 ± 5 ppm. To maintain stable gas concentration, three high-precision mass flow meters (accuracy of 0.01 mL/min) were used in the VOCs flow, high purity nitrogen flow, and mixture flow. All standard gas of nitrogen, toluene, n-hexane, and ethyl acetate were provided by Guangzhou Kewenda Trading Co., Ltd. All of the adsorbents were pretreated by heating at 120 °C for 10 h in vacuum before use.

2.3.2. *Breakthrough curves*

Breakthrough curves present the dimensionless concentration, $C/C_{0\%}$, as a function of time at the outlet of the glass reactor. The $C/C_0\%$ was calculated using Eq. (1):

$$C\Big/C_0\% = \frac{Gas_{(in)}}{Gas_{(out)}} \times 100\% \tag{1}$$

where $Gas_{(in)}$ and $Gas_{(out)}$ are the inlet and outlet concentrations of the VOC gas.

The adsorption capacity (q, $mg{\cdot}g^{-1}$) of the adsorbent was calculated based on the breakthrough curve using Eq. (2) (Liu et al., 2021):

$$q = \frac{V}{1000m}\left(C_0 t - \int_0^t C_t d_t\right) \tag{2}$$

where C_0 and C_t ($mg{\cdot}L^{-1}$) represent the concentrations of the target pollutant gas at the inlet and outlet, respectively; V is the volumetric flow rate ($mg{\cdot}L^{-1}$) of the gas; m (g) is the mass of adsorbent; and t (min) represents the adsorption time. All breakthrough curves were tested at room temperature.

2.4. *Adsorption curve analysis methods*

2.4.1. *Adsorption kinetics*

The pseudo-first-order equation using Eq. (3) (Xu et al., 2020):

$$\log(q_e - q_t) = \log q_e - \frac{k_1}{2.303} t \tag{3}$$

where k_1 is the kinetic rate constant of pseudo-first-order adsorption (min^{-1}), and q_e and q_t ($mg{\cdot}g^{-1}$) represent the amounts of adsorption at equilibrium and time t (min), respectively.

The pseudo-second-order equation is given as Eq. (4) (Zaman et al., 2020):

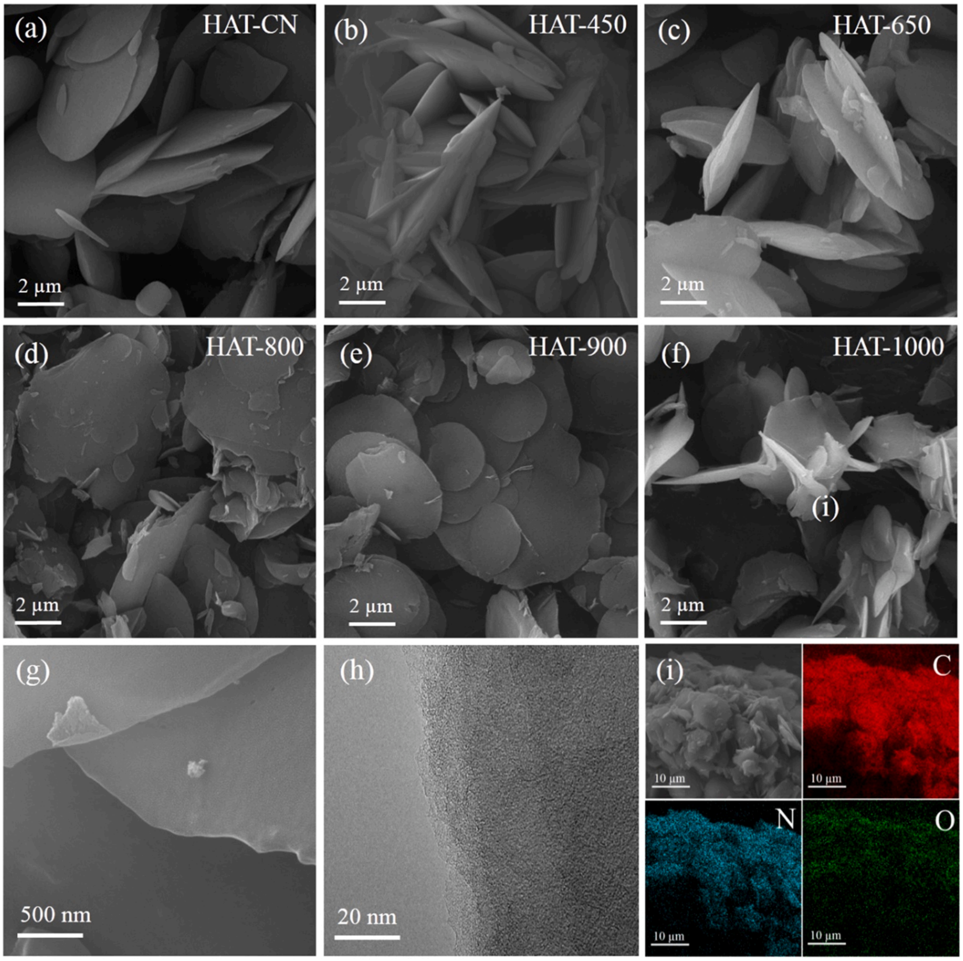

Fig. 3. SEM images of (a) HAT-CN, (b) HAT-450, (c) HAT-650, (d) HAT-800, (e) HAT-900, (f) HAT-1000, (g) TEM image of HAT-650, (h) HRTEM image of HAT-650, (i) SEM mapping of HAT-650.

$$\frac{t}{q_t} = \frac{1}{k_2 q_e^2} + \frac{t}{q_e} \tag{4}$$

where k_2 is the kinetic rate constant of pseudo-second-order adsorption (g·mg^{-1}·min^{-1}), q_e and q_t have the same meaning as the above.

The adsorption kinetics may alternatively be described from a mechanistic point of view. A diffusion-controlled adsorption process can be explored by using the intra-particle diffusion model. Intra-particle diffusion model usually include 3 steps, the first straight portion represents that surface diffusion is mainly affected by mass transfer, the second depicts pores diffusion, and the third indicates interior surface diffusion (Wang et al., 2020; Allen et al., 1989). The intra-particle diffusion model can be expressed as Eq. (5) (Wang et al., 2020):

$$q_t = k_{id} t^{0.5} + \theta \tag{5}$$

where k_{id} is the intra-particle diffusion rate constant (mg·g^{-1}·min$^{-0.5}$), and θ (mg·g^{-1}) is a constant related to the thickness of the boundary layer.

2.4.2. Isotherm model

The Langmuir model is based on the hypothesis that the monolayer adsorption occurs onto a surface with a finite number of identical sites, which is commonly given as Eq. (6) (Yang et al., 2017):

$$q_e = \frac{q_m k_L C_e}{1 + k_L C_e} \tag{6}$$

where Ce (mg m^{-3}) is the concentration at equilibrium, q_e (mg·g^{-1}) is the equilibrium adsorption capacity, k_L (m^3·mg^{-1}) and q_m (mg·g^{-1}) are the Langmuir constant and theoretical maximum adsorption capacity, respectively.

2.5. Desorption & regeneration

The desorption experiment starts after the adsorption equilibrium. Dry flowing air with a rate of 30 mL/min was used as a purge gas. In this work, heating was used to release VOCs and regenerate adsorbents synchronously. During the desorption process, the adsorption materials were heated by a small heating furnace. The desorbed gas was monitored by an online gas chromatography to measure the desorption efficiency. Based on the desorption curve, desorption capacity of the adsorbent was calculated using Eq. (7) (Liu et al., 2021):

$$q = \frac{V}{1000m} \int_0^t C_t d_t \tag{7}$$

where C_t is the concentration of VOCs at the outlet; V is the volumetric flow rate (mg·L^{-1}) of the gas; m (g) is the mass of adsorbents; and t (min) represents the desorption time.

3. Results and discussion

3.1. Characterizations of the adsorbents

The crystal phase of the synthesized HAT-Xs (HAT-450, HAT-650, HAT-800, HAT-900, and HAT-1000) were obtained by XRD (Fig. 2a).

Table 1
Elemental compositions of HAT-Xs from XPS and EDS.

Samples		HAT-450	HAT-650	HAT-800	HAT-900	HAT-1000
O Atom %	XPS	5.85	4.56	7.27	4.82	5.03
	EDS	3.94	1.49	2.12	2.52	3.41
C Atom %	XPS	61.15	65.32	68.97	82.56	87.06
	EDS	49.97	58.80	68.81	79.33	81.41
N Atom %	XPS	33	30.12	22.06	12.62	6.93
	EDS	46.10	39.71	29.07	18.15	15.18
	Graphitic	31.19	32.53	35.86	42.20	50.74
	Pyridinic	26.96	32.29	28.62	26.61	19.12
	Pyrrolic	41.32	30.75	24.55	14.36	11.22
	N-O	0.53	4.42	10.97	16.83	18.92
C/N	XPS	1.85	2.16	3.12	6.54	12.56

The broad characteristic peak of C (002) at 26.73° indicates the amorphous structure carbon material, shifts to 25.68° with the synthesis temperature increased to 1000 °C. It is noteworthy that the full width at half maximum (FWHM) of XRD profiles of (002) peak decreases from 19.02 to 5.95, which indicates a highly crystalline graphite-like carbon structure (Zhang et al., 2020). As shown in Fig. 2(b), compared to pure HAT-CN, HAT-450 and HAT-650 still have a certain amount of function groups, like –OH, -C-O, -C≡N, and –N-O. The functional groups of carbon materials may have an important influence on organic compounds adsorption (Eris and Bashiri, 2019). The high synthesis temperature results in fewer surface functional groups for HAT-800, HAT-900, and HAT-1000.

The TGA-IR test was carried out to study the influence of temperature on the material composition of HAT-CN. As shown in the TGA profile (Fig. 2c) and 3D images of the IR spectra (Fig. S1a, Fig. 2d), a main weight loss appeared at the temperature of 525 °C, mainly due to the loss of –C≡N groups at the edges of the carbon molecule (Walczak et al., 2018). The IR transmission spectra of the vapor release from pure HAT-CN with decomposition temperature increasing from 25 to 1000 °C are shown in Fig. 2(d) and Fig. S1b. The peaks appear at 1201, 1226, and 1338 cm^{-1}, which can be attributed to deformation vibrations and stretching vibrations of C–O–C, and deformation vibration of C–N, respectively (Zhou et al., 2014; Wang et al., 2015; Shafiei et al., 2018). As shown in Fig. 2(d), HAT-650 has fewer C–O–C and C–N function groups compared to HAT-450. The functional groups of the substrate continuously decrease when the synthesis temperature exceeds 650 °C.

The SEM images (Fig. 3) show that HAT-Xs have a disc-like stacked layered structure with an average diameter of about 7 µm and an average thickness of 150 nm. Compared to HAT-CN, the structure of HAT-Xs collapse during the annealing process. With the synthesis temperature increased, the layer structure agglomeration occurs. The surface of HAT-CN is smooth and clean, while much small debris appeared on the surface of HAT-800, HAT-900, and HAT-1000. The TEM (Fig. 3g) and HRTEM images (Fig. 3h) further reveal an amorphous layered structure of HAT-650, which is consistent with the XRD. The SEM mapping image of HAT-650 is shown in Fig. 3(i) and the elemental compositions from the EDS and XPS are presented in Table 1.

XPS spectra were used to identify the elements, relative content, and bonding types of HAT-Xs. The XPS survey spectra, C1s spectra, and N1s spectra of HAT-Xs were shown in Fig. S2, Fig. S3, and Fig. 4, respectively. As shown in Fig. S2, the HAT-Xs were mainly composed of carbon, nitrogen, and oxygen. The oxygen content is relatively constant, around 5 atom% (Table 1). The atom% content of C increased from 61.15% to 87.06%, while N decreased from 33% to 6.93% (Table 1) with the temperature increasing from 450 to 1000°C during the synthesis process, which is consistent with the loss of nitrogen-containing function groups in the IR results. It is worth noting that the C/N ratios of HAT-450 and HAT-650 are close to 2/1, which means that they are similar to the C_2N-type carbon-nitride. Deconvolution of the N1s spectra (Fig. 4) reveals that the peaks at 398, 399, 400.5, and 402.5 eV, correspond to pyridinic N, pyrrolic N, graphitic N, and oxidized nitrogen, respectively (Walczak et al., 2018). With increasing carbonization temperatures, the total N content and the pyrrolic N decreased, while the graphitic N increased. The asymmetric state of the electron cloud of pyrrolic N endows it a great potential to coordinate with organic molecules, which can improve the adsorption of carbon-nitride materials to VOC molecules (Zhang et al., 2020; Sun et al., 2020). It is worth mentioning that

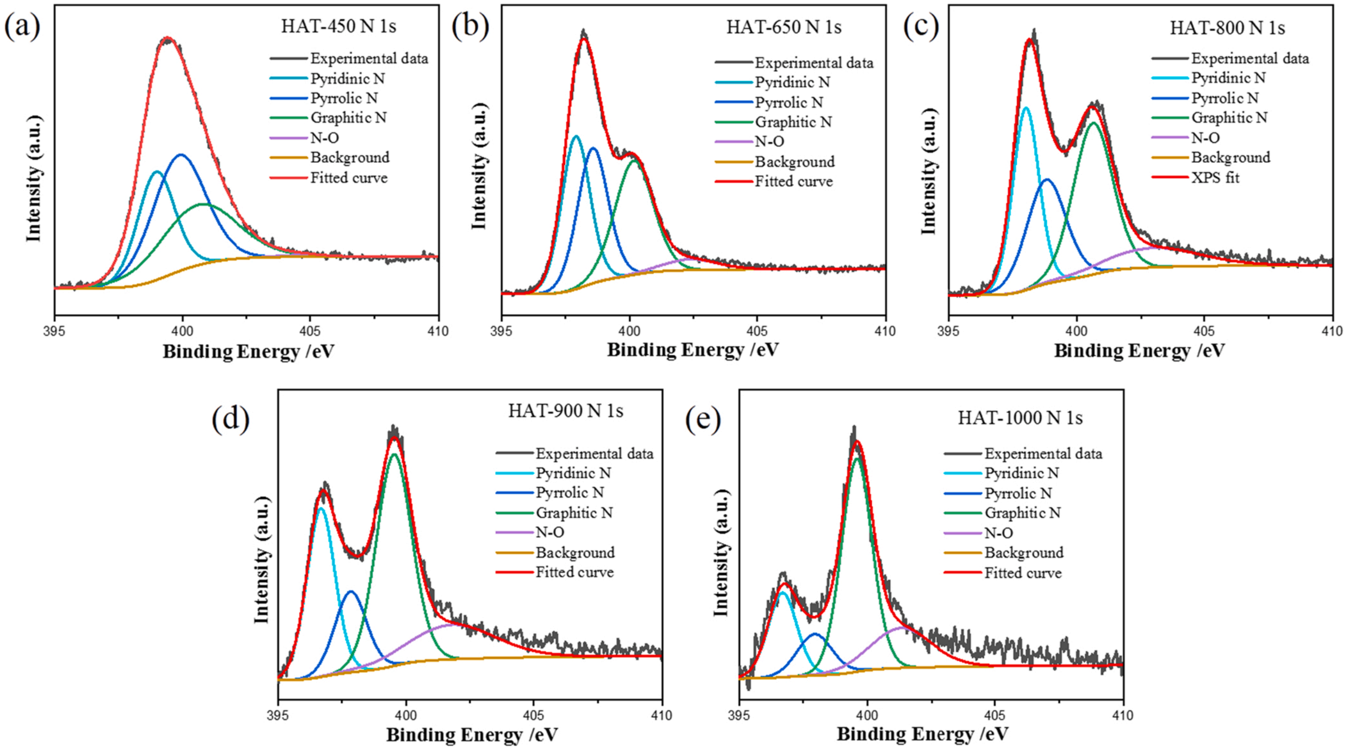

Fig. 4. N1s spectra of HAT-Xs: (a) HAT-450, (b) HAT-650, (c) HAT-800, (d) HAT-900, and (e) HAT-1000.

Table 2
BET surface area and pore structure of HAT-Xs.

Samples	BET surface area ($m^2 \cdot g^{-1}$)	Total pore volume ($cm^3 \cdot g^{-1}$)	Pore diameter (nm)
HAT-450	6.0	0.03	19.6
HAT-650	305.7	0.22	2.8
HAT-800	206.4	0.13	2.6
HAT-900	48.9	0.07	5.6
HAT-1000	30.4	0.05	7.1

HAT-650 has the highest content of pyridinic N of 32.29%. The pyridinic N content increased at first and then gradually decreased, and the turning point appeared at 650 °C. Deconvolution of the C1s spectra (Table 1 and Fig. S3) reveal that the peaks at 284, 285, 286, and 290 eV, belong to graphitic C, sp^2-hybridized C–N, sp^3-hybridized C–N, and C–O bond, respectively (Walczak et al., 2018). With the increase of synthesis temperature, the content of graphitic C increased, while sp^2-hybridized C–N and sp^3-hybridized C–N decreased. Due to the higher C content and higher graphitic C ratio, the samples synthesized at higher temperatures exhibit a higher graphitization degree, which is consistent with the XRD.

The specific surface areas of HAT-Xs were characterized by nitrogen adsorption–desorption isotherms, as shown in Fig. S4. A large amount of N_2 adsorption occurred at low pressure ($P/P_0 < 0.1$) and hysteresis loops appeared at high pressure, corresponding to type-I and type-Ⅳ isotherms, which indicated that there are both micropores and mesopores in the materials (Kim and Ahn, 2012). The BET surface area and pore structure of HAT-Xs were list in Table 2. The pore size distribution plots of HAT-Xs were shown in Fig. S4b–f. The HAT-Xs mainly illustrated pores with a size of 0.3 ~1 nm except HAT-450. From the previous IR results, there are abundant function groups in the layer and porous structure, which caused the low specific surface area and large pore diameter of HAT-450. HAT-650 shows a small average pore size of 2.84 nm and a high surface area of 305.7 m^2 g^{-1}, which is promoting adsorption capacity (Zhang et al., 2017). The specific surface areas of HAT-800, HAT-900 and HAT-1000 gradually decreased, which is due to the structural collapse at high temperature as demonstrated by the TEM images in Fig. 3.

3.2. *Adsorption performance of the HAT-Xs*

3.2.1. *The different adsorption performances of the HAT-Xs*

Ethyl acetate adsorption performance of the HAT-Xs were measured by the breakthrough curves with a gas concentration of 150 ± 5 ppm at ambient temperature. As shown in Fig. 5(a) and Table S1, the adsorption got breakthrough for all the HAT-Xs samples. HAT-450 showed a poor adsorption performance and low adsorption capacity for ethyl acetate, which may be due to the lower specific surface area compared to other adsorbents. HAT-650 showed the best adsorption performance with the breakthrough ($C/C_0\% < 10\%$) time of 290 min, and an adsorption capacity of 140.97 mg g^{-1}, which is about 3.26 times as high as that for HAT-800 (43.17 mg g^{-1}). It is worth mentioning that, as shown in

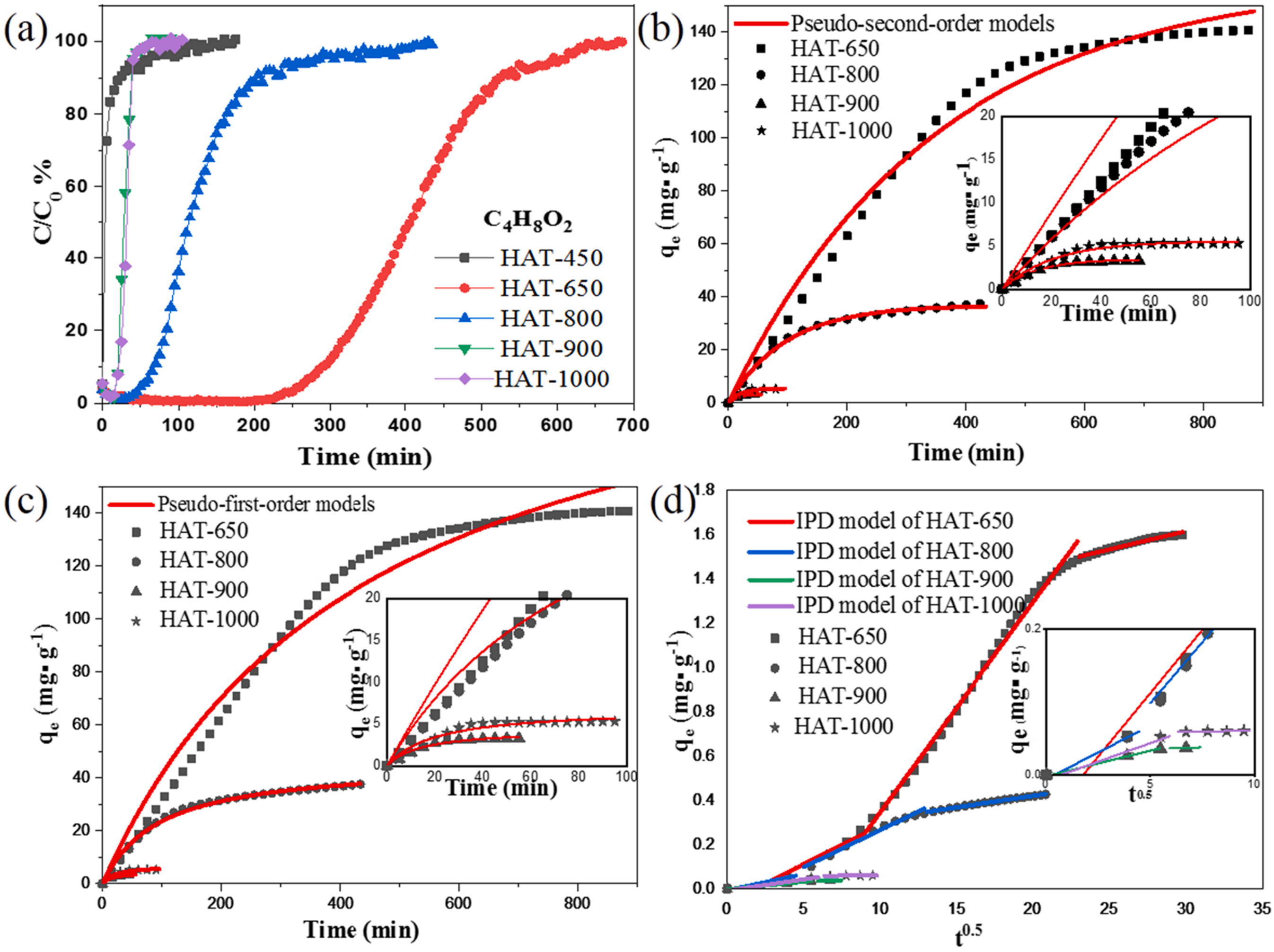

Fig. 5. (a) The breakthrough curves of ethyl acetate onto HAT-Xs. Kinetic modeling for the adsorption of ethyl acetate onto HAT-650, HAT-800, HAT-900 and HAT-1000, (b) pseudo-first-order, (c) pseudo-second-order, and (d) intra-particle diffusion (IPD) modelling.

Table 3
Parameters of pseudo-first-order, pseudo-second-order and intra-particle diffusion kinetic models for the adsorption of ethyl acetate onto HAT-650, HAT-800, HAT-900 and HAT-1000, with the gas concentration of 150 ± 5 ppm at room temperature.

Samples			HAT-650	HAT-800	HAT-900	HAT-1000
Pseudo first order	q_e	$(mg \cdot g^{-1})$	160.5	36.9	3.4	5.5
	k_1	(min^{-1})	0.0029	0.0103	0.0718	0.485
	R^2		0.984	0.996	0.991	0.976
Pseudo Second order	q_e	$(mg \cdot g^{-1})$	228.7	46.1	4.4	6.9
	k_2	$(g \cdot mg^{-1} \cdot min^{-1})$	0.00001	0.0002	0.0157	0.0071
	R^2		0.974	0.993	0.977	0.951
intra-particle diffusion	k_{id}	$(mg \cdot g^{-1} \cdot min^{-0.5})$	1.4	0.010	0.0071	0.010
	θ	$(mg \cdot g^{-1})$	98.7	0.21	-0.0024	-0.0077
	R^2		0.971	0.966	0.971	0.938

Fig. S6a, the adsorption capacity of HAT-650 for ethyl acetate is 3.2 times for that of commercial activated carbon (44.13 $mg \cdot g^{-1}$). With the synthesis temperature increased from 650 to 1000°C, the adsorption capacity gradually decreased, which matches the variation of specific surface area (Table 2). The largest specific area, highest N content and a suitable amount of functional groups are the possible reasons for HAT-650 to be the best gas adsorbent.

The adsorption kinetics is important to study the mechanism of the adsorption process (Eris and Bashiri, 2019; Antuña-Nieto et al., 2020; Tang et al., 2015). Therefore, different mathematical models including pseudo-first-order, pseudo-second-order and intra-particle diffusion models had been used to analyze the breakthrough curves of ethyl acetate adsorption on HAT-650, HAT-800, HAT-900 and HAT-1000.

The plots of pseudo-first-order and pseudo-second-order kinetic models for the adsorption of ethyl acetate onto HAT-650, HAT-800, HAT-900 and HAT-1000 were shown in Fig. 5(b) and (c), and the parameters were summarized in Table 3. Compared to pseudo-second-order, the correlation coefficients (R^2) of pseudo-first-order were more close to 1, indicating that the pseudo-first-order model are fitting the adsorption well, and the adsorption of ethyl acetate onto the HAT-Xs is a physical adsorption process (Eris and Bashiri, 2019; Yadav et al., 2019). Moreover, the isotherms measured at 290, 292, 294, and 296 K were shown in Fig. S5, and the isosteric heat of adsorption (Qst) was calculated to be 18.8 ~24.5 KJ mol^{-1}, which can also confirm the ethyl acetate adsorption on HAT-650 is a physical adsorption process (Chen et al., 2016; An and Rosi, 2010). As shown in Table 3, the highest equilibrium adsorption capacity, q_e, by pseudo-first-order and lowest adsorption rate constant (k_1) prove the best adsorption performance of HAT-650 (Eris and Bashiri, 2019).

The R^2 values for the intra-particle diffusion model were higher than 0.93, meaning that the intra-particle diffusion model is suitable for data-fitting. As shown in Fig. 5(d), the data exhibit two or three linear lines, indicating that there are two or three controlling steps for the adsorption process (Wu et al., 2009). The k_{id} is the rate of adsorption, the higher value means higher intra-particle mass transfer rate. In this work, we use the lowest k_{id} value as the final value in Table 3, which indicates that the rate-determining step (Bang and Kim, 2017). For HAT-650 and HAT-800, the rate determination step appears in the third place, while for HAT-900 and HAT-1000, the rate determination step is in the second place. For the small specific surface area (below 50 m^2 g^{-1}, Table 2) and low total pore volume (below 0.1 cm^3 g^{-1}, Table 2) of HAT-900 and HAT-1000, the adsorption on interior surface is difficult to proceed.

3.2.2. *The adsorption performance of HAT-650 for toluene, n-hexane and ethyl acetate*

Typical VOCs including toluene, n-hexane, and ethyl acetate were chosen as the target pollutant gases to investigate the adsorption performance of HAT-650. The breakthrough curves of toluene, n-hexane, and ethyl acetate as the target pollutant gases are shown in Fig. 6(a), Fig. S6, and Table S1. The adsorption capacity of HAT-650 for ethyl acetate reached 140.97 m^2 g^{-1}, which is about 3.58 times higher for n-hexane (39.43 m^2 g^{-1}), and 2.90 times higher for toluene (48.61 m^2 g^{-1}). As shown in Table S1, all the HAT-Xs samples show excellent adsorption selectivity to ethyl acetate, and the gas adsorption capacities of the HAT-Xs for toluene, n-hexane, and ethyl acetate follow an order of HAT-650 > HAT-800 > HAT-900 > HAT-1000 > HAT-450, which also matches the order of specific surface area (Table 2).

The adsorption isotherms of HAT-650 for toluene, n-hexane, and ethyl acetate are presented in Fig. 6(b) and Table S2. All the isotherms were well fitted to the Langmuir model with the correlation coefficients

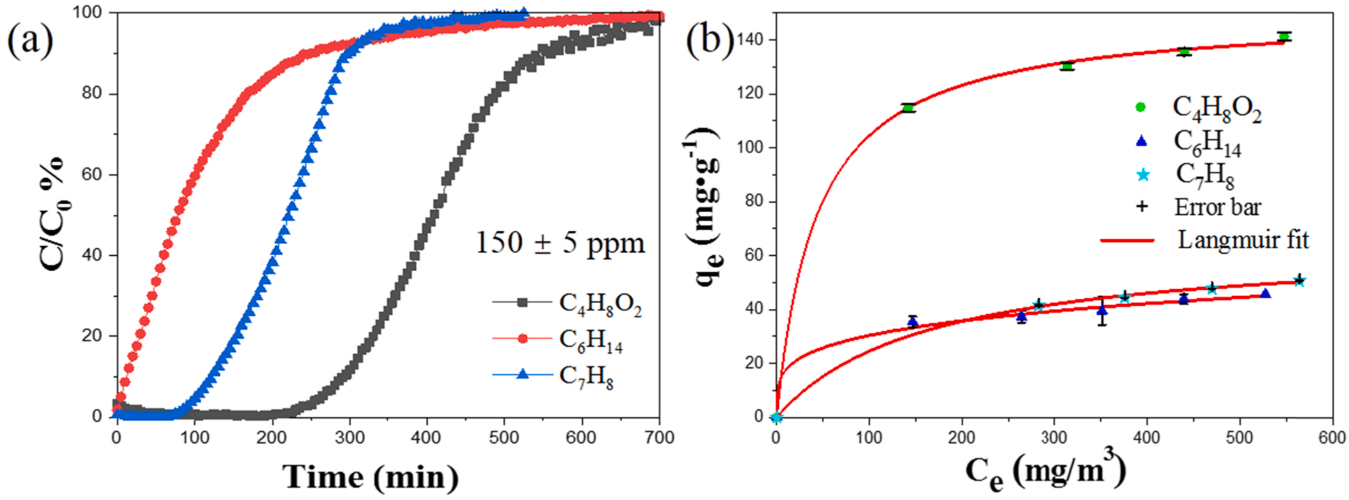

Fig. 6. (a) The breakthrough curves of toluene (C_7H_8), n-hexane (C_6H_{14}), and ethyl acetate ($C_4H_8O_2$) onto HAT-650 with a gas concentration of 150 ± 5 ppm; (b) adsorption isotherms of toluene, n-hexane and ethyl acetate onto HAT-650, and non-linear fits of the Langmuir model.

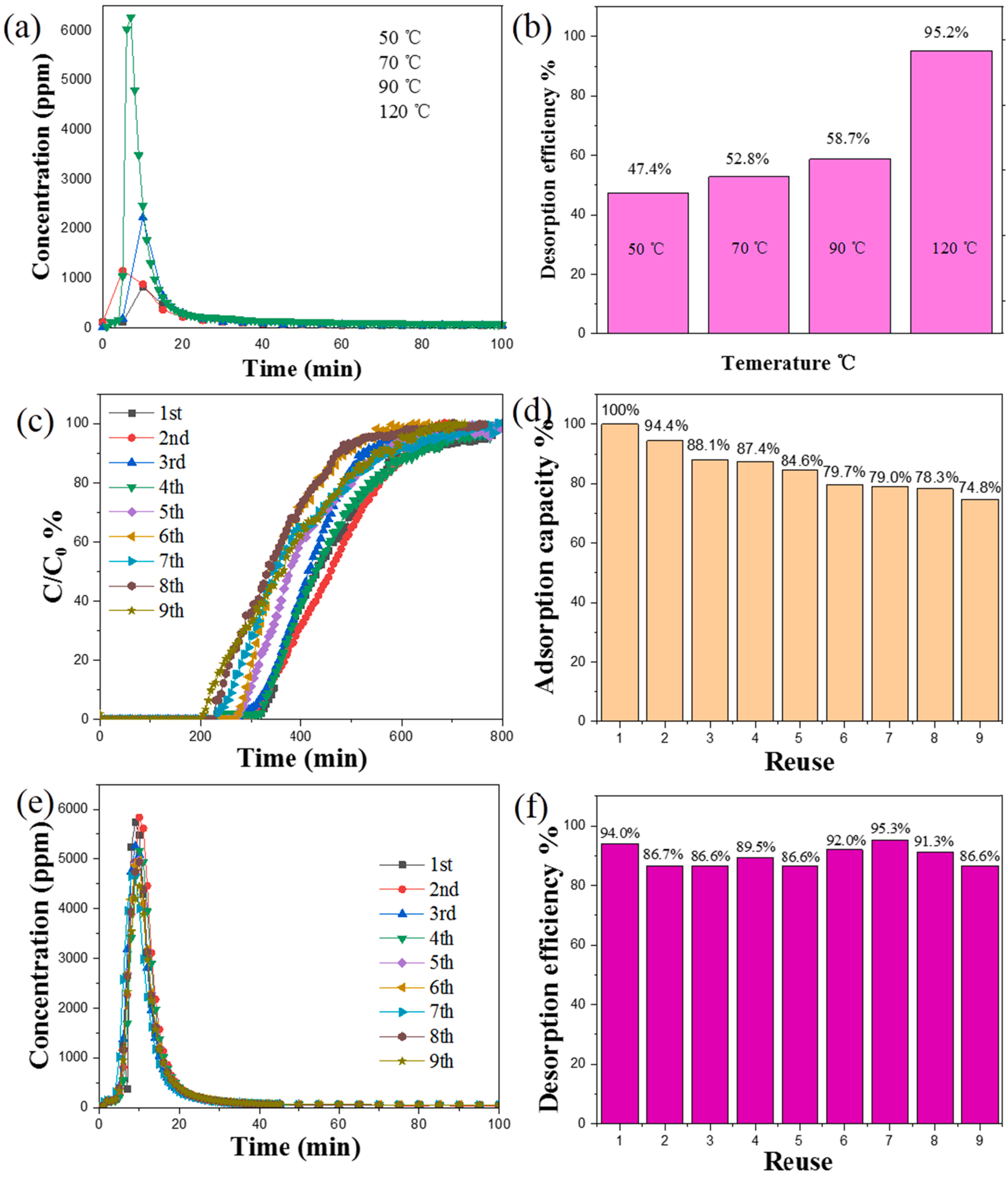

Fig. 7. (a) Desorption curves in different temperature and (b) desorption efficiency, cyclic performance of ethyl acetate adsorption breakthrough curves (c) and (d) adsorption capacity, (e) desorption curves, (f) desorption efficiency.

(r^2)≧ 0.990, indicating a monolayer reversible adsorption process of the VOCs onto HAT-650. Notably, the calculated maximum adsorption capacities (q_m) of ethyl acetate is 150 mg g^{-1}, which is ~2.9 times of n-hexane (52 mg g^{-1}), and ~2.3 times of toluene (64 mg g^{-1}), respectively. The intra-particle diffusion model was used to study the diffusion of toluene, n-hexane, and ethyl acetate on HAT-650. As shown in Fig. S7 and Table S3, for all the VOCs, the rate determination steps appeared in the third place. In both three places, the adsorption rate k_{id} of ethyl acetate is 1.455 mg g^{-1} $min^{-0.5}$, which is more than 140 times to that of toluene and n-hexane. It means that the diffusion of ethyl acetate on HAT-650 is easier than any other VOC molecules. On one hand, the molecular diameter of ethyl acetate (4.95 Å) (Manjare and Ghoshal,

2006) is smaller than toluene (5.68 Å) (Song et al., 2008), which can help ethyl acetate enter the pores of the carbon-nitrides easily and may lead to a smoother adsorption process (Wang et al., 2012a). On the other hand, the carbon-based adsorbents can interact with the C═O function of ethyl acetate via hydrogen bonding and form strong physical adsorption (Bang and Kim, 2017; Cross and Rochester, 1979). In addition, the polarizability of ethyl acetate (1.7) (Schaep et al., 1999) is higher than toluene (0.4) and n-hexane (0.1) (Bruggen et al., 2002), which induces stronger electrostatic and dispersion interaction with the adsorbent (Yi et al., 2012). Therefore, HAT-650 presents a good adsorption capacity of ethyl acetate.

3.2.3. *Desorption & regeneration & reuse*

In this work, the desorption efficiencies of HAT-650 for ethyl acetate at different temperatures were tested. As shown in Fig. 7(a) and (b), at different temperatures, desorption process mainly appeared in the first 30 min, and more than 67% ethyl acetate is desorbed. As the desorption temperature increases from 50° to 120°C, the desorption efficiency increases from 47.4% to 95.2%. When the temperature reached 120 °C, the outlet concentration of ethyl acetate rapidly ascended to the highest point of 6287 ppm within 10 min. The rapid desorption rate and high desorption efficiency make the adsorbed ethyl acetate easy to collect. At the same time, the low desorption temperature reduces energy consumption, making HAT-650 promising in industrial applications. Table S4 summarized the thermal desorption and regeneration of different carbon-based VOCs adsorbents, the HAT-650 has a lower desorption temperature.

Reusability is also an important factor in the practical application of adsorbents. Different from some adsorbents which need another regeneration progress after desorption (Das et al., 2004; Chen et al., 2021), the HAT-650 sample can be regenerated by the desorption process. As shown in Fig. 7(c) and (d), five cycles have been tested. After the first cycle of desorption and regeneration, HAT-650 displayed a relatively high adsorption capacity of ethyl acetate at 139.02 mg g^{-1}, which was 98.61% of the initial adsorption capacity (140.98 mg g^{-1}). After 9 regeneration cycles, the adsorption capacity still kept 74.8% of the first cycle, and the desorption efficiency all higher than 86% in 9 cycles. The results demonstrated that HAT-650 presents excellent stability and reusability for ethyl acetate removal.

4. Conclusion

In summary, disc-like structured nitrogen-rich porous carbon materials (HAT-Xs) were synthesized by a simple one-step annealing method using HAT-CN as the precursor. After annealing at different temperatures, HAT-Xs exhibit different morphology and physical properties. The adsorption kinetics suggest that the adsorption of ethyl acetate onto HAT-Xs is a physical adsorption process, and the interior surface diffusion is the main rate-determining step. HAT-650 shows the best adsorption performance for ethyl acetate with the experimental adsorption capacity of 140.97 mg g^{-1}, which is 3.2 times for that of commercial activated carbon. And it also shows excellent reusability with a low desorption/regeneration temperature of 120 °C, high desorption efficiency of 95.2%, and 74.8% of the initial adsorption capacity after nine cycles. Thus, HAT-650 is a promising adsorbent for industrial applications. The discussion of the mechanism in this article is not deep enough, and more research on the mechanism of selective adsorption is needed. In the future, the HAT-650 could also be used in the gas separation due to its significant ethyl acetate gas selectivity. In addition, due to its high specific surface area and abundant surface function groups, it may have promising application prospects as catalysts or catalyst carriers.

CRediT authorship contribution statement

Li Tan: Investigation, Data curation, Formal analysis, Writing – original draft. **Jiangen Wang:** Formal analysis, Writing – review & editing. **Bihai Cai:** Formal analysis. **Chengyin Wang:** Writing – review & editing. **Zhimin Ao:** Conceptualization, Supervision, Funding acquisition, Validation, Writing – review & editing. **Shaobin Wang:** Supervision, Writing – review & editing.

Declaration of Competing Interest

The authors declare the following financial interests/personal relationships which may be considered as potential competing interests: Zhimin Ao reports financial support was provided by National Natural Science Foundation of China, Science and Technology Planning Project of Guangdong Province, and the Innovation Team Project of Guangdong Provincial Department of Education.

Acknowledgements

This work was supported by the National Natural Science Foundation of China (No. 21777033, 22176041), China Postdoctoral Science Foundation (No. 2020M672538), Science and Technology Planning Project of Guangdong Province (No. 2017B020216003), and Innovation Team Project of Guangdong Provincial Department of Education (No. 2017KCXTD012).

Appendix A. Supporting information

Supplementary data associated with this article can be found in the online version at doi:10.1016/j.jhazmat.2021.127348.

References

Allen, S.J., Mckay, G., Khader, K.Y.H., 1989. Intraparticle diffusion of a basic dye during adsorption onto sphagnum peat. Environ. Pollut. 56, 39–50.

Antuña-Nieto, C., Rodríguez, E., López-Antón, M.A., García, R., Martínez-Tarazona, M.R., 2020. Mercury adsorption in the gas phase by regenerable Au-loaded activated carbon foams: a kinetic and reaction mechanism study. New J. Chem. 44, 12009–12018.

An, J., Rosi, N.L., 2010. Tuning MOF CO_2 adsorption properties via cation exchange. J. Am. Chem. Soc. 132, 5578–5579.

Azhagapillai, P., Vijayanathan Pillai, V., Al Shoaibi, A., Chandrasekar, S., 2020. Selective adsorption of benzene, toluene, and m-xylene on sulfonated carbons. Fuel 280, 118667.

Bang, S.-Y., Kim, J.-H., 2017. Isotherm, kinetic, and thermodynamic studies on the adsorption behavior of 10-deacetylpaclitaxel onto Sylopute. Biotechnol. Bioprocess Eng. 22, 620–630.

Bathen, D., 2003. Physical waves in adsorption technology—an overview. Sep. Purif. Technol. 33, 163–177.

Bruggen, B., Geens, J., Vandecasteele, C., 2002. Fluxes and rejections for nanofiltration with solvent stable polymeric membranes in water, ethanol and n-hexane. Chem. Eng. Sci. 57, 2511–2518.

Chabot, V., Higgins, D., Yu, A., Xiao, X., Chen, Z., Zhang, J., 2014. A review of graphene and graphene oxide sponge: material synthesis and applications to energy and the environment. Energy Environ. Sci. 7, 1564.

Chen, K.J., Madden, D.G., Pham, T., Forrest, K.A., Kumar, A., Yang, Q.Y., Xue, W., Space, B., Perry, J.J., Zhang, J.P., Chen, X.M., Zaworotko, M.J., 2016. Tuning pore size in square-lattice coordination networks for size-selective sieving of CO_2. Angew. Chem. Int. Ed. 55, 10268–10272.

Chen, L., Yuan, J., Li, T., Jiang, X., Ma, S., Cen, W., Jiang, W., 2021. A regenerable N-rich hierarchical porous carbon synthesized from waste biomass for H2S removal at room temperature. Sci. Total Environ. 768, 144452.

Cross, S., Rochester, C.H., 1979. Infrared study of the adsorption of ethyl acetate on silica immersed in carbon tetrachloride. J. Chem. Soc. 75, 2865–6868.

Das, D., Gaur, V., Verma, N., 2004. Removal of volatile organic compound by activated carbon fiber. Carbon 42, 2949–2962.

Davidson, C.J., Hannigan, J.H., Bowen, S.E., 2021. Effects of inhaled combined Benzene, Toluene, Ethylbenzene, and Xylenes (BTEX): toward an environmental exposure model. Environ. Toxicol. Pharmacol. 81, 103518.

Duan, X., Xu, J., Wei, Z., Ma, J., Guo, S., Wang, S., Liu, H., Dou, S., 2017. Metal-free carbon materials for CO_2 electrochemical reduction. Adv. Mater. 29, 1701784.

Eris, S., Bashiri, H., 2019. Kinetic study of the adsorption of dyes onto activated carbon. Prog. React. Kinet. Mech. 41, 109–119.

Gang, D., Uddin Ahmad, Z., Lian, Q., Yao, L., Zappi, M.E., 2021. A review of adsorptive remediation of environmental pollutants from aqueous phase by ordered mesoporous carbon. Chem. Eng. J. 403, 126286.

González-Martín, J., Kraakman, N.J.R., Pérez, C., Lebrero, R., Muñoz, R., 2021. A state–of–the-art review on indoor air pollution and strategies for indoor air pollution control. Chemosphere 262, 128376.

Guo, Y., Wen, M., Li, G., An, T., 2021. Recent advances in VOC elimination by catalytic oxidation technology onto various nanoparticles catalysts: a critical review. Appl. Catal. B: Environ. 281, 119447.

Gwenzi, W., Chaukura, N., Wenga, T., Mtisi, M., 2021. Biochars as media for air pollution control systems: Contaminant removal, applications and future research directions. Sci. Total Environ. 753, 142249.

Kim, K.-J., Ahn, H.-G., 2012. The effect of pore structure of zeolite on the adsorption of VOCs and their desorption properties by microwave heating. Microporous Mesoporous Mater. 152, 78–83.

Kong, X.-K., Chen, C.-L., Chen, Q.-W., 2014. Doped graphene for metal-free catalysis. Chem. Soc. Rev. 43, 2841–2857.

Kou, Y., Xu, Y., Guo, Z., Jiang, D., 2011. Supercapacitive energy storage and electric power supply using an aza-fused π-conjugated microporous framework. Angew. Chem. Int. Ed. 50, 8753–8757.

Liu, H., Xu, M., Li, G., Zhang, W., An, T., 2021. Solar-light-triggered regenerative adsorption removal of styrene by silver nanoparticles incorporated in metal–organic frameworks. Environ. Sci.: Nano 8, 543–553.

Liu, B., Zhao, W., Jiang, Q., Ao, Z., An, T., 2019. Enhanced adsorption mechanism of carbonyl-containing volatile organic compounds on Al-decorated porous graphene monolayer: a density functional theory calculation study. Sustain. Mater. Technol. 21, e00103.

Li, D., Ning, X.-a, Huang, Y., Li, S., 2019. Nitrogen-rich microporous carbon materials for high-performance membrane capacitive deionization. Electrochim. Acta 312, 251–262.

Mahmood, J., Lee, E.K., Jung, M., Shin, D., Jeon, I.-Y., Jung, S.-M., Choi, H.-J., Seo, J.-M., Bae, S.-Y., Sohn, S.-D., Park, N., Oh, J.H., Shin, H.-J., Baek, J.-B., 2015. Nitrogenated holey two-dimensional structures. Nat. Commun. 6, 6486.

Manjare, S.D., Ghoshal, A.K., 2006. Comparison of adsorption of ethyl acetate on activated carbon and molecular sieves 5A and 13X. J. Chem. Eng. Data 51, 1185–1189.

Nguyen, C., Do, D.D., 1998. Adsorption of benzene and ethanol on activated carbon, MCM-41 and Zeolite Y. Adsorpt. Sci. Technol. 16, 439–452.

Oh, G.-Y., Ju, Y.-W., Jung, H.-R., Lee, W.-J., 2008. Preparation of the novel manganese-embedded PAN-based activated carbon nanofibers by electrospinning and their toluene adsorption. J. Anal. Appl. Pyrolysis 81, 211–217.

Pan, B., Xing, B., 2008. Adsorption mechanisms of organic chemicals on carbon nanotubes. Environ. Sci. Technol. 42, 9005–9013.

Qiu, K., Yang, L., Lin, J., Wang, P., Yang, Y., Ye, D., Wang, L., 2014. Historical industrial emissions of non-methane volatile organic compounds in China for the period of 1980–2010. Atmos. Environ. 86, 102–112.

Schaep, J., Wilms, D., Vandecasteele, C., 1999. Influence of molecular size, polarity and charge on the retention of organic molecules by nanofiltration. J. Membr. Sci.

Sciorio, R., Rapalini, E., Esteves, S.C., 2021. Air quality in the clinical embryology laboratory: a mini-review. Ther. Adv. Reprod. Health 15, 1–11.

Shafiei, M., Alivand, M.S., Rashidi, A., Samimi, A., Mohebbi-Kalhori, D., 2018. Synthesis and adsorption performance of a modified micro-mesoporous MIL-101(Cr) for VOCs removal at ambient conditions. Chem. Eng. J. 341, 164–174.

Song, W.Lee, Jae, K.Cheon, Heung, J.Park, Min, G.Lee, 2008. Adsorption characteristics of binary vapors among acetone, MEK, benzene, and toluene. Korean J. Chem. Eng. 25, 1154–1159.

Sun, Z., Zhao, L., Liu, C., Zhen, Y., Ma, J., 2020. Fast adsorption of BPA with high capacity based on π-π electron donor-acceptor and hydrophobicity mechanism using an in-situ sp2C dominant N-doped carbon. Chem. Eng. J. 381, 122510.

Tang, L., Zhang, S., Zeng, G.-M., Zhang, Y., Yang, G.-D., Chen, J., Wang, J.-J., Wang, J.-J., Zhou, Y.-Y., Deng, Y.-C., 2015. Rapid adsorption of 2,4-dichlorophenoxyacetic acid by iron oxide nanoparticles-doped carboxylic ordered mesoporous carbon. J. Colloid Interface Sci. 445, 1–8.

Uchimiya, M., Wartelle, L.H., Lima, I.M., Klasson, K.T., 2010. Sorption of deisopropylatrazine on broiler litter biochars. J. Agric. Food Chem. 58, 12350–12356.

Walczak, R., Kurpil, B., Savateev, A., Heil, T., Schmidt, J., Qin, Q., Antonietti, M., Oschatz, M., 2018. Template- and metal-free synthesis of nitrogen-rich nanoporous "noble" carbon materials by direct pyrolysis of a preorganized hexaazatriphenylene precursor. Angew. Chem. Int. Ed. 57, 10765–10770.

Wang, H., Jahandar Lashaki, M., Fayaz, M., Hashisho, Z., Philips, J.H., Anderson, J.E., Nichols, M., 2012a. Adsorption and desorption of mixtures of organic vapors on beaded activated carbon. Environ. Sci. Technol. 46, 8341–8350.

Wang, H., Maiyalagan, T., Wang, X., 2012b. Review on recent progress in nitrogen-doped graphene: synthesis, characterization, and its potential applications. ACS Catal. 2, 781–794.

Wang, H., Sun, Y., Zhu, T., Wang, W., Deng, H., 2015. Adsorption of acetaldehyde onto carbide-derived carbon modified by oxidation. Chem. Eng. J. 273, 580–587.

Wang, J., Yi, H., Tang, X., Zhao, S., Gao, F., 2020. Simultaneous removal of SO_2 and NOx by catalytic adsorption using γ-Al_2O_3 under the irradiation of non-thermal plasma: competitiveness, kinetic, and equilibrium. Chem. Eng. J. 384, 123334.

Wu, F.-C., Tseng, R.-L., Juang, R.-S., 2009. Initial behavior of intraparticle diffusion model used in the description of adsorption kinetics. Chem. Eng. J. 153, 1–8.

Xu, X., Zhang, S., Tang, J., Pan, L., Eguchi, M., Na, J., Yamauchi, Y., 2020. Nitrogen-doped nanostructured carbons: A new material horizon for water desalination by capacitive deionization. Energy Chem. 2, 100043.

Yadav, S., Singh, S., Goel, N., Singhal, S., 2019. Investigations on functionalized GO as selective and efficient amino acids carrier supported by density functional calculations. Appl. Surf. Sci. 497, 143761.

Yang, C., Miao, G., Pi, Y., Xia, Q., Wu, J., Li, Z., Xiao, J., 2019. Abatement of various types of VOCs by adsorption/catalytic oxidation: a review. Chem. Eng. J. 370, 1128–1153.

Yang, Z., Yi, H., Tang, X., Zhao, S., Yu, Q., Gao, F., Zhou, Y., Wang, J., Huang, Y., Yang, K., Shi, Y., 2017. Potential demonstrations of "hot spots" presence by adsorption-desorption of toluene vapor onto granular activated carbon under microwave radiation. Chem. Eng. J. 319, 191–199.

Yi, H., Deng, H., Tang, X., Yu, Q., Zhou, X., Liu, H., 2012. Adsorption equilibrium and kinetics for SO_2, NO, CO_2 on zeolites FAU and LTA. J. Hazard. Mater. 203–204, 111–117.

You, J., Zhang, C., Wu, Z., Ao, Z., Sun, W., Xiong, Z., Su, S., Yao, G., Lai, B., 2021. N-doped graphite encapsulated metal nanoparticles catalyst for removal of Bisphenol A via activation of peroxymonosulfate: A singlet oxygen-dominated oxidation process. Chem. Eng. J. 415, 128890.

Yue, X., Ma, N.L., Sonne, C., Guan, R., Lam, S.S., Van Le, Q., Chen, X., Yang, Y., Gu, H., Rinklebe, J., Peng, W., 2021. Mitigation of indoor air pollution: a review of recent advances in adsorption materials and catalytic oxidation. J. Hazard. Mater. 405, 124138.

Zaman, A., Orasugh, J.T., Banerjee, P., Dutta, S., Ali, M.S., Das, D., Bhattacharya, A., Chattopadhyay, D., 2020. Facile one-pot in-situ synthesis of novel graphene oxide-cellulose nanocomposite for enhanced azo dye adsorption at optimized conditions. Carbohydr. Polym. 246, 116661.

Zhang, X., Gao, B., Creamer, A.E., Cao, C., Li, Y., 2017. Adsorption of VOCs onto engineered carbon materials: a review. J. Hazard. Mater. 338, 102–123.

Zhang, Z., Yu, L., Tu, Y., Chen, R., Wu, L., Zhu, J., Deng, D., 2020. Unveiling the active site of metal-free nitrogen-doped carbon for electrocatalytic carbon dioxide reduction. Cell Rep. Phys. Sci. 1, 100145.

Zheng, X., Zhang, H., Rehman, S., Zhang, P., 2021. Energy-efficient capture of volatile organic compounds from humid air by granular metal organic gel. J. Hazard. Mater. 411, 125057.

Zhou, X., Huang, W., Shi, J., Zhao, Z., Xia, Q., Li, Y., Wang, H., Li, Z., 2014. A novel MOF/graphene oxide composite GrO@MIL-101 with high adsorption capacity for acetone. J. Mater. Chem. A 2, 4722–4730.

Zhu, J., Zhan, H.-L., Zhao, K., Miao, X.-Y., Zhou, Q., Yue, W.-Z., 2019. Competitive and synergistic adsorption of binary volatile organic compound mixtures on activated carbon. Chin. Phys. B 28, 020204.